AIAA JOURNAL
Vol. 58, No. 8, August 2020

Coherence Analysis of the Noise from a Simulated Highly Heated Laboratory-Scale Jet

Kevin M. Leete* and Kent L. Gee†
Brigham Young University, Provo, Utah 84602
Junhui Liu‡
U.S. Naval Research Laboratory, Washington, D.C. 20375
and
Alan T. Wall§
U.S. Air Force Research Laboratory, Wright–Patterson Air Force Base, Ohio 45433

https://doi.org/10.2514/1.J059112

Measurements of full-scale high-performance military aircraft reveal phenomena that are not widely seen at laboratory scales. However, recent modifications to large eddy-simulation (LES) methods allow for simulations of jets operating at a high-temperature ratio in a similar regime as military aircraft operating at afterburner. This work applies coherence analyses that have been previously used to study the jet noise field produced by military aircraft to the LES of a highly heated laboratory-scale jet. The coherence of the complex pressures along a near-field line approximately parallel to the shear layer as well as along the nozzle lip line shows evidence of distinct noise production mechanisms that transfer information differently from the flow to the field. A phenomenological comparison between the LES and measurements of an afterburning F-35 aircraft is then made. Although the LES is not run at the exact same conditions as the aircraft and does not reproduce all of the phenomena present in the aircraft's jet noise field, differences between noise production mechanisms observed in the LES may describe some of the spatiospectral lobe phenomena observed in the measurements of the F-35.

Nomenclature

D	=	jet nozzle diameter
f	=	frequency, Hz
G_{xx}	=	autospectra of signal x
G_{xy}	=	cross spectra between signals x and y
M	=	local Mach number
m	=	number of elements in an array
n	=	number of measurement blocks
$\boldsymbol{P}$	=	$m \times n$ matrix of complex pressures at a single frequency for an array
U	=	fluid velocity, m/s
U_j	=	jet velocity, m/s
x, y, z	=	Cartesian coordinates with origin at the nozzle exit and x axis along the jet centerline, m
$\boldsymbol{\Gamma}^2(f)$	=	coherence matrix of an array for frequency f
γ	=	ratio of specific heats
$\gamma^2(f)$	=	frequency-dependent coherence function
$\epsilon[\gamma^2]$	=	normalized random error of the calculation of γ^2
λ	=	acoustic wavelength, m

I. Introduction

THE primary source of noise from high-performance military aircraft is the turbulent mixing of the jet exhaust with the ambient air. The complex nature of this sound source results in noise radiated to the aft of the aircraft that has spatially dependent characteristics: the aft radiation has significant spatial coherence and a peaked spectrum, whereas the radiation more toward the sideline has a broader spectrum with low coherence. Because these two main field regions were found to be consistent between many laboratory-scale jets of different shapes, sizes, and speeds, Tam et al. [1] were able to generate similarity spectra fitted to the shape of the measured spectra in the two regions.

To connect the far-field acoustics to the measured jet flow, two-point correlation techniques have been used on laboratory-scale jets [2–5]. This, along with the development of visualization methods [6,7] of the flow, led to the understanding that the two field regions are attributed to two general noise production mechanisms: fine-scale turbulent structures, and large-scale turbulent structures. Fine-scale turbulent structures are understood as small eddies or other perturbations in the mixing region of the flow, which exert an effective turbulence pressure on their surroundings [8,9]. Large-scale turbulence structures are understood as Kelvin–Helmholtz instability waves generated in the shear layer of the jet at the nozzle [10], which grow as they move downstream. A useful framework for understanding the time-harmonic radiation of the coherent structures is in terms of a wave-packet model, which has a growth, saturation, and decay of amplitude over space as well as a phase relationship [11]. If the phase velocity across the wave packet is supersonic compared to ambient conditions, sound is radiated efficiently to the far field at an angle related to the phase velocity. If the phase velocity is subsonic, the finite size of the wave packet causes wave-number leakage, ultimately resulting in only portions of the energy being radiated to the far field.

A difficulty in understanding jet noise has appeared when recent measurement of three different military aircraft [12–14] showed deviations from the two-source model in the aft radiation of the jet noise. Neilsen et al. [15,16] and Tam et al. [14] observed errors in similarity spectra fits due to the measurements of the aircraft containing multiple peaks in the spectra of the aft radiation. To investigate the multiple peaks spectra of the F-35 [13], Leete et al. [17] used multisource statistically optimized near-field acoustical holography to reconstruct the pressure field surrounding the aircraft. They found that the region of maximum radiation can be represented as a superposition of several "spatiospectral" lobes. Spatiospectral lobes are local maxima in the space-frequency domain, where the spectra from multiple measurements across space are plotted side by side.

Presented as Paper 2019-2633 at the 25th AIAA/CAES Aeroacoustics Conference, Delft, The Netherlands, May 20–23, 2019; received 2 October 2019; revision received 21 February 2020; accepted for publication 31 March 2020; published online 13 May 2020.

*Ph.D. Candidate, Department of Physics and Astronomy. Student Member AIAA.
†Professor of Physics, Department of Physics and Astronomy. Senior Member AIAA.
‡Mechanical Engineer. Senior Member AIAA.
§Research Physicist, Battlespace Acoustics Branch, 2610 Seventh St., Bldg. 441. Member AIAA.

Subsets of these phenomena are observed as a dual-peaked spectrum at a single microphone location in the field (such as observed in Refs. [14,15]) or a split directivity pattern in space at a single frequency. The relative amplitudes and spatiospectral slopes of the multiple lobes, which can vary greatly with engine condition, determine the directivity and peak frequency(ies) of the jet noise. Some evidence for these multiple spatiospectral lobes are observed even in engine powers as low as 25% engine thrust request (ETR) for the F-35 [17].

Correlation and coherence analysis applied to field measurements of military aircraft [18,19] have been useful in characterizing the spatiospectral lobes. Harker et al. [18] showed that the signals recorded in the region of maximum overall sound pressure level (OASPL) of a rectangular-nozzled afterburning aircraft have significant correlation with two different time delays, implying that there are two sets of waves with different phase speeds propagating across the array, resulting in different far-field directivities. For the F-35, Swift et al. [19] showed that the lobes in the spatiospectral domain are mutually incoherent, and there is a measurable coherence between the broadband shock-associated noise (BBSAN) radiating upstream with the spatiospectral content in the aft radiation.

There have been limited reported observations of what could be considered spatiospectral lobes in measurements of laboratory-scale jets. Seiner et al. reported multiple peaks in the directivity in the OASPL as well as at specific Strouhal numbers in Figs. 13 and 17 of Ref. [20] for a jet of total temperature ratio of 5.4. Another example is seen in the right pane of Fig. 7 of Ref. [21], where a spatiospectral map of the sound pressure levels measured at a dense array parallel to the jet centerline showed maxima and minima. It is unknown if the phenomenon has gone largely unreported because laboratory-scale jets do not operate at the conditions required to produce the lobes (high temperature, Mach number, complicated nozzle geometry, etc.) or because many experiments do not sufficiently resolve the spatiospectral domain to observe it.

Large-eddy simulations (LESs) of turbulent jets afford the opportunity to produce a finely sampled spatiospectral domain in the radiated noise as well as simultaneous details about the flow. Efforts in the field over many years have allowed for the increasing accuracy in noise predictions [22,23]. Within this large body of simulation work, a focus on the use of the simulations to gain insight on noise source mechanisms is abundant. This is generally accomplished by using various decomposition methods [24] to search for coherent wave-packet-like structures, whose radiation can then be interpreted more readily. Some of these methods include data-driven decompositions such as the field into acoustic, hydrodynamic, and thermal modes using Doak's momentum potential theory [25]; the spectral proper orthogonal decomposition (SPOD) [26]; and dynamic mode decomposition [27]. Additionally, operator-based analysis such as global linear stability analysis [28] and resolvent analysis [29,30] can add information about cause and effect relationships within the flow and between the flow and acoustic radiation.

Adaptation of LESs to accurately represent conditions of full-scale military aircraft is an ongoing challenge. Liu et al. [31–33] adapted the U.S. Naval Research Laboratory's Jet Engine Noise Reduction (JENRE®), finite element LES solver to simulate temperatures similar to conditions of high-performance military aircraft at afterburner. Spatiospectral domain analysis of the aft radiation shows a smooth transition from high-frequency components peaking with a directivity at at jet inlet angle of about 115 deg to lower-frequency content with a farther aft directivity of about 140 deg [32]. Based on instantaneous pressure maps of the field, they identify the higher-frequency upstream content as Mach wave radiation due to its plane-wave-like unidirectional behavior. The lower-frequency content that radiates at larger aft angles has a more stochastic radiation pattern with a less defined directivity, which they describe as large-scale turbulent structure noise. This distinction between Mach wave radiation and large-scale turbulent structure noise is new because, often, those terms are used interchangeably. Although these LESs of jet noise with a temperature ratio of seven remain unvalidated due to lack of experimental data at that temperature, other LES studies at that temperature ratio reported similar findings [34,35].

Another example of multiple different source mechanisms contributing to the aft radiation in jet noise is found in the SPOD and resolvent analysis undertaken by Schmidt et al. [26]. They showed the shape and location of modes at frequencies where the field energy is dominated by low-rank behavior. In general, these were shown to fall into two categories: Kelvin–Helmholtz type, and Orr [36] type. The Kelvin–Helmholtz-type wave-packet structures are present in the shear region, starting near the nozzle exit, and have a high phase velocity; whereas the Orr-type wave packets are present after the end of the potential core spread over a larger region with a lower phase velocity. With these observations of Schmidt et al. [26] and Liu et al. [32], it then becomes a question of if these source mechanisms are responsible for the spatiospectral lobe behavior of full-scale military aircraft operating at afterburner.

Since flow measurements are not available for operating military aircraft, flow decomposition techniques to understand source phenomena are not possible, and thus a more roundabout method is needed to understand potential acoustic sources. The goal of this paper is to apply coherence analysis methods previously used to characterize the noise fields of high-performance military aircraft at afterburner [18,19] to the large-eddy simulations of a laboratory-scale jet operating at a temperature ratio of seven [32] to understand if the high temperature in the LES can produce spatiospectral lobe content. Of particular interest is the separation of the field and the flow into different regions, the characterization of their properties, and then using the coherence between the flow and the field to understand possible noise production mechanisms. Then, spectral and coherence data from an F-35 [13,19] jet noise field are phenomenologically compared to the LES for potential explanations of the spatiospectral lobe phenomena observed in that aircraft.

II. LES of the Highly Heated Laboratory-Scale Jet

The LES dataset used in this work is provided by Liu et al. [31–33], who used the Jet Engine Noise Reduction solver to calculate the heated flow passing through a convergent/divergent nozzle. The JENRE® solver uses a monotonically integrated LES approach with a flux-corrected transport algorithm [37] and explicit Taylor–Galerkin scheme. Tetrahedral meshes were used to implement the complicated nozzle geometry, which had a nozzle exit diameter D of 2.868 in., a design Mach number of 1.5, and a fully expanded pressure ratio of 3.7. The thermodynamic quantities in the flow region were calculated out to a conical surface outside of the main flow; then, the far-field pressures were predicted using the Ffowcs Williams and Hawkings integration method [38]. Cell sizes of about $D/286$ were used near the nozzle lip, which gradually increased to around $D/20$ near the Ffowcs Williams and Hawkings integration surface. Specifics of the choice of integration surface and grid resolutions can be found in Ref. [39].

The simulation was run for at a nozzle pressure ratio of four, a temperature ratio of seven, and a Mach number (referenced to the ambient condition) of 3.38, resulting in an underexpanded, shock containing jet with a temperature in the same regime as high-performance military aircraft operating at afterburner [40]. A method for calculating the temperature-dependent specific heat ratio was incorporated, which was found to match well with National Institute of Standards and Technology (NIST)[¶] databases for air under these conditions (see Fig. 2 of Ref. [32]). Time records of the LES were split into 97 blocks, and a Fourier transform was applied to each block to give a complex pressure spectrum with a frequency spacing of about 150 Hz. Since the accuracy of the coherence calculation is dependent on the number of simulated measurement blocks and the frequency spacing in the spectra is dependent on the length of each block, it was necessary to run this simulation for much longer than generally is sufficient for analyses of the LES. The total temporal duration of the simulation was 0.326 s, which covers 5260 convective time units (D/U_J). The nozzle geometry and a representative pressure field at the test condition used in this study can be seen in Fig. 1. Superimposed on the instantaneous pressure map of Fig. 1 is the location of the Ffowcs Williams and Hawkings integration surface (FWHS; solid black lines).

[¶]NIST Chemistry WebBook: http://webbook.nist.gov/chemistry/; https://doi.org/10.18434/T4D303.

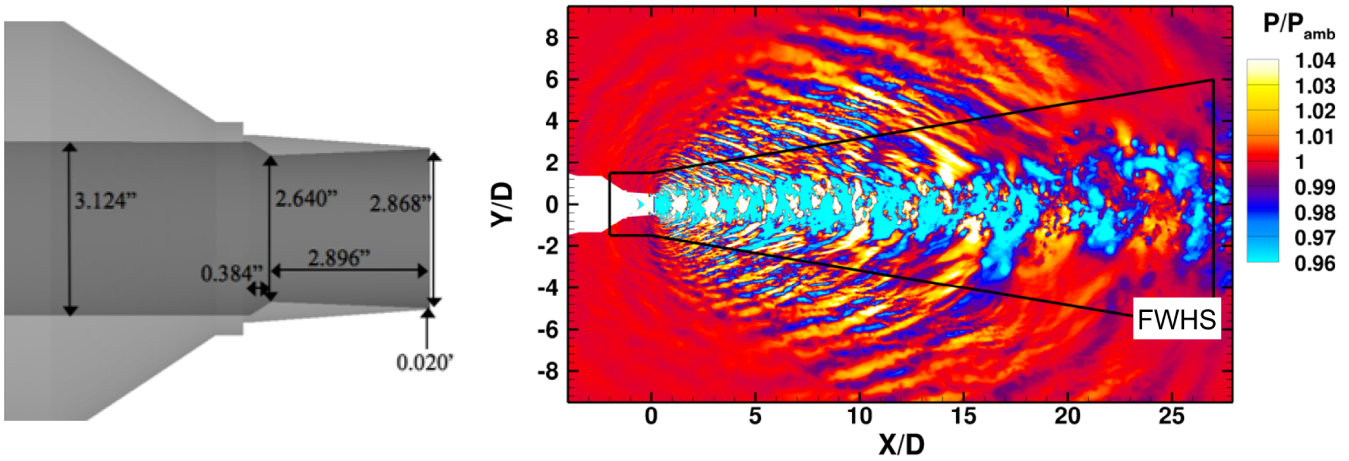

Fig. 1 Nozzle geometry (left) and representative pressure field of LES (right). Solid lines show the FWHS.

Figure 2 includes a schematic of the simulation with the nozzle exit, the Ffowcs Williams and Hawkings integration surface, and two simulated arrays where the field was sampled. The red and blue diamonds show the locations of the ends of the potential and supersonic cores, respectively. All lengths are nondimensionalized by the exit diameter D, with the flow in the positive x direction and the origin at the center of the nozzle exit. The flowfield was sampled along the nozzle lip line of the jet from the nozzle exit to $x/D = 25$. The acoustic field was sampled along the line $y/D = (1/6)x/D + 10$, from $x/D = -10$ to $x/D = 40$. The right panel of Fig. 2 shows the local Mach number of the fluid along the jet centerline (blue) and the ratio of the fluid velocity U to the jet velocity U_j (red). The end of the potential core is estimated as $x/D = 7.2$, where $U/U_j \approx 0.95$ (dashed line) and is marked with a red diamond. The end of the supersonic core is located at $x/D = 12.67$, where $M = 1$ and is marked with a blue diamond.

The normalized sound pressure levels along the field array are pictured in the left pane of Fig. 3. The spectra from each simulated array point between 0 and 7 kHz is shown. On the left, upstream of the nozzle exit, broadband shock-associated noise is seen starting at about 3.5 kHz and shifting up in frequency to 7 kHz at about $x/D = 5$. Overall levels are the highest between $5D$ and $30D$, where the directional portion of the turbulent mixing noise is present. From $x/D = 5$ to $x/D \approx 9$, the peak frequency of the spectrum decreases approximately as $1/x$; whereas from $x/D \approx 9$ to the end of the array, the peak frequency decreases approximately as $1/x^2$. The far-field peak in the OASPL is at an inlet angle of 115 deg.

Work to use LES to predict radiated jet noise fields at these extreme temperatures is ongoing [34,35,41]. Because of lack of laboratory-scale experimental data at these high temperatures, direct validation of the simulation at a temperature ratio of seven has not been completed. However, the LES methodology has been validated up

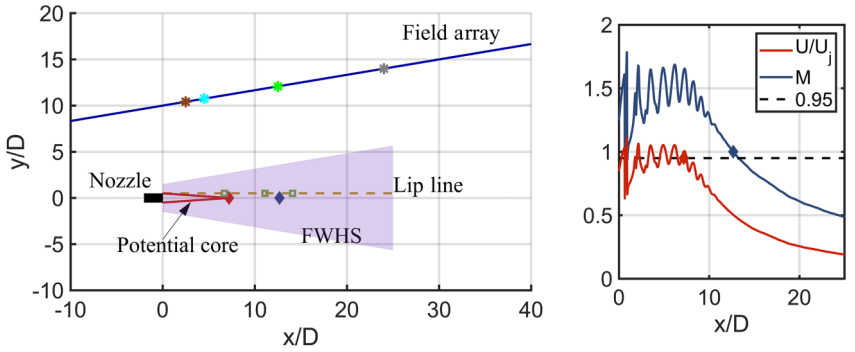

Fig. 2 Schematic of nozzle exit location, two simulated measurement arrays used in this paper, FWHS, and approximate location of the potential core (left); and Mach number and jet velocity ratio along jet centerline (right).

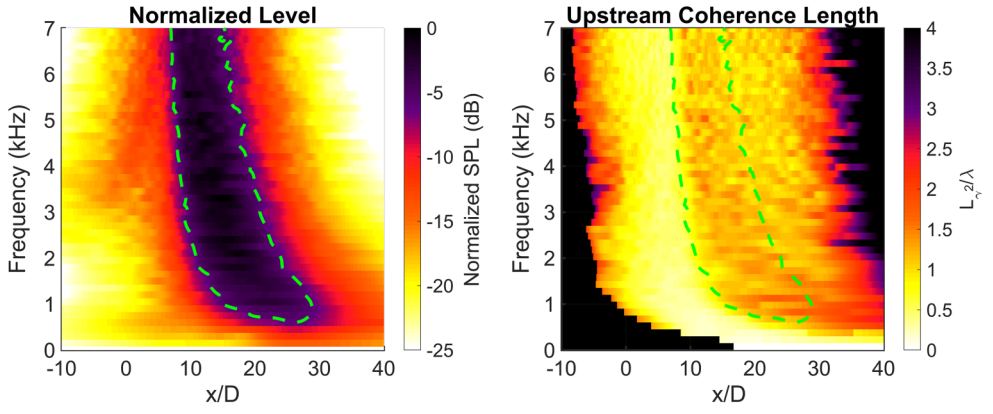

Fig. 3 Normalized sound pressure level (SPL) and coherence lengths along the simulated field array between 0 and 7 kHz.

to a temperature ratio of three (similar to military aircraft operating at full power without afterburner) [32], and the peak directivity angle of the aft radiation (115 deg) agrees well with a predicted value of 112 deg based on Tam's vortex sheet model for Mach wave radiation [42]. Additionally, Chen and Mihaescu [35], in their simulations of jets at a temperature ratio of seven, showed spatiospectral trends in the far-field that qualitatively match those seen here.

III. Coherence Analysis

A. Coherence Function

The frequency-dependent coherence function $\gamma^2(f)$ is a frequency-domain analog of the correlation function, and it is defined as

$$\gamma^2(f) = \frac{|G_{xy}(f)|^2}{G_{xx}(f)G_{yy}(f)} \tag{1}$$

where G_{xx} and G_{yy} are the autospectra of arbitrary signals x and y, and G_{xy} is their cross spectrum. The coherence is restricted to range $0 \leq \gamma^2 \leq 1$, where a value of one signifies that all of the time-averaged energy in y is linearly related to the energy in x at that frequency; and a value of zero means there is no relation. For two measurement arrays, x and y, the complex pressures are arranged into $m \times n$ (m being the number of elements in the array and n the number of blocks) matrices $\boldsymbol{P}_x$ and $\boldsymbol{P}_y$. A coherence matrix $\boldsymbol{\Gamma}^2(f)$, whose entries are the $\gamma^2(f)$ between all combinations of points on two measurement arrays, is calculated by

$$\boldsymbol{\Gamma}^2(f) = \frac{|\boldsymbol{P}_x\boldsymbol{P}_y^{\mathrm{H}}|^2}{\mathrm{diag}(\boldsymbol{P}_x\boldsymbol{P}_x^{\mathrm{H}})\mathrm{diag}(\boldsymbol{P}_y\boldsymbol{P}_y^{\mathrm{H}})^{\mathrm{H}}} \tag{2}$$

where $\mathrm{diag}(\cdot)$ signifies extracting the main diagonal of the argument matrix as a column vector, and the magnitude squared $|\cdot|^2$ and division operations are done elementwise. The ith row of $\boldsymbol{\Gamma}^2(f)$ is the coherence between the element x_i and all of the y_j, and the reverse is true for the columns. If x and y are the same array, $\boldsymbol{\Gamma}^2(f)$ is symmetric, square, and the values along the diagonal are unity.

In the work of Bendat and Piersol [43], equation 9.82 gave the normalized random error of the coherence calculation $\epsilon[\gamma^2]$, which is reproduced here as Eq. (3):

$$\epsilon[\gamma^2] \approx \frac{\sqrt{2}(1-\gamma^2)}{\sqrt{n}\sqrt{\gamma^2}} \tag{3}$$

The error is a function of the calculated coherence itself as well as the inverse square root of the number of blocks n. For the number of blocks used in this study, a coherence estimation of less than $\gamma^2 = 0.02$ results in a $\epsilon[\gamma^2]$ value greater than one, meaning the true coherence could be, in fact, zero. This gives a practical lower limit to the possible values of γ^2 obtainable in this study, and all plots are limited to show values above this threshold.

A valuable measure of coherence that is often used is the coherence length L_{γ^2}, which in this work is calculated as the distance between two points along an array in which the γ^2 drops from unity to 0.5. The concept of coherence lengths has been useful for wave-packet models [44,45] to construct equivalent acoustic sources for jet noise. For comparison across multiple frequencies, L_{γ^2} is normalized by the acoustic wavelength, as was done by Swift et al. [19]. If L_{γ^2}/λ is small such that γ^2 decays rapidly over space, it is often necessary to interpolate the calculation of γ^2 between array points to reach an estimation of the true value of L_{γ^2}.

B. Field Coherence

The coherence matrix of a measurement array in the vicinity of a jet gives insight into the jet noise field properties. Since $\boldsymbol{\Gamma}^2(f)$ is a large matrix for each frequency, it is difficult to concisely visualize trends across frequencies. The coherence length L_{γ^2} then becomes a useful visualization tool. If L_{γ^2} is calculated in a single direction, it allows for a single value to be plotted for each frequency and array position, which can then be displayed in a single figure. Figure 3 shows the normalized sound pressure levels along the field array and the corresponding upstream ($-x$ direction) L_{γ^2}/λ. The plot is saturated to black at four or when there are not enough upstream microphones in the array to mark a drop in coherence to 0.5. The dashed line marks the level contour 6 dB down from the maximum and is repeated on the plot of the upstream coherence lengths for reference. This spatiospectral region is referred to as the region of maximum radiation in this work.

In Fig. 3, the largest values of L_{γ^2}/λ are found aft of $x/D = 30$, which appears to be due to the array being large compared to the aeroacoustic source, causing the propagating acoustic waves to impinge at grazing incidence. When this occurs, the coherence along subsequent points in the array are large, as the information in the field is transported along the array. Upstream of $x/D = 0$, L_{γ^2}/λ is large in the 3–5 kHz band where the BBSAN signature is seen and increases toward the edge of the array. Coherence lengths are the lowest at about $x/D = 10$, where the radiation toward the sideline is broadband. In the maximum radiation region, coherence lengths generally stay between one to two wavelengths. At 0.5–1.5 kHz, there is a general increase in L_{γ^2}/λ downstream of $20D$, which continues to the end of the array. As frequency drops to zero and wavelengths become very large compared to the dimensions of the jet flow, normalized coherence lengths naturally drop to zero.

Although L_{γ^2} serves as a useful glance at the entire field in one plot, the full story of the field is only told by analysis of $\boldsymbol{\Gamma}^2(f)$. A single column of $\boldsymbol{\Gamma}^2(f)$ can be extracted for each frequency and compiled to create a coherence spectra of the array to the reference point corresponding to the chosen column. Figures 4a–4d display the coherence spectrum of the array with respect to four reference points located at $x/D = 2.5, 4.5, 12.5$, and 24, respectively. These points were chosen to represent phenomenological trends observed as the coherence was examined for all points along the array. The vertical dotted lines represent the location of the reference, and their colors match the four

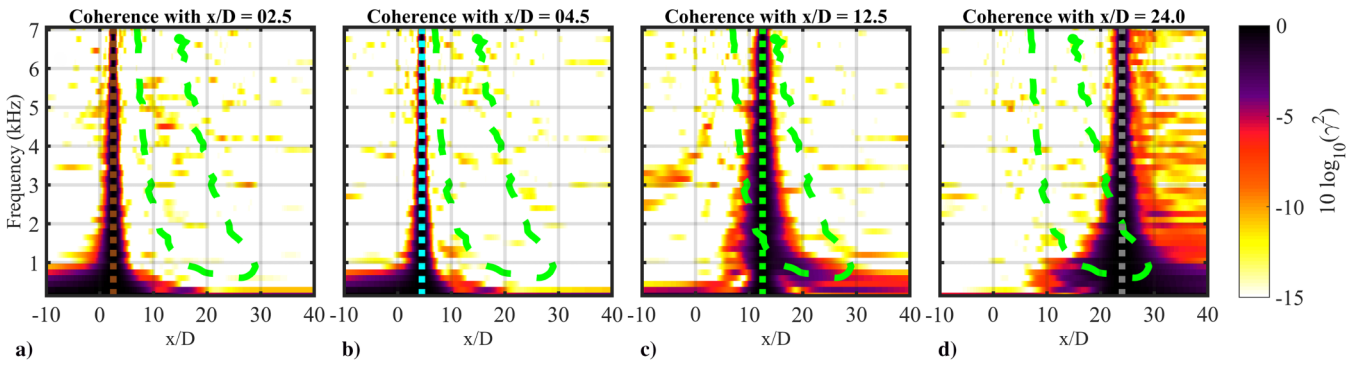

Fig. 4 Coherence of field array with four different reference points along it: $x/D = 2.5, 4.5, 12.5$, and 24. Colored dotted lines represent reference locations and correspond to colored asterisks in Fig. 2.

asterisks marked on the field array in Fig. 2. The coherence spectrum in Fig. 4a uses a reference chosen where the BBSAN signature is observed in Fig. 3. Faint traces of coherence can be seen between the reference point and 10D downstream between 4 and 6 kHz. This faint trace of coherence is in the frequency range where the BBSAN level is the largest at the reference. Figure 4b shows the coherence spectrum with a reference point chosen where the coherence lengths in Fig. 3 were the lowest, just upstream of the region of maximum radiation. The coherence is small across all but the lowest frequencies.

Figure 4c shows the coherence of the array with a reference located in the maximum radiation region. The coherence is generally larger than seen in Figs. 4a and 4b, as well as over a larger spatial extent, as is seen by the increase in L_γ^2/λ in Fig. 3. What is unseen in Fig. 3 is that, in the region of maximum radiation, a single point in space contains frequency information that is coherent with the upstream BBSAN signature. Coherence between the BBSAN and the region of maximum radiation implies that either the BBSAN source is propagating downstream into the region of maximum radiation as well as upstream or the source mechanisms (BBSAN source and the source contributing the region of maximum radiation) are not independent. An example of the sources not being independent could be if the actuation of the shock cells by instability waves [46] were to transfer some of the shock fluctuation information to the acoustic field via their Mach wave radiation. The coherence alone cannot distinguish between these two possible explanations. Swift et al. [19] showed a similar pattern with their coherence analysis of the F-35.

Figure 4d shows that, as the reference point is moved farther downstream, the coherence of the field increases with a larger increase in the 0.5 to 1.5 kHz range. Even though the reference is not completely removed from the region of maximum radiation, any evidence of coherence with the BBSAN disappears. It is possible this is caused by some change in the source mechanism responsible for the radiation to the field in that direction, although there is some common coherence between Figs. 4c and 4d below 1 kHz. The coherence for frequencies above 1 kHz begins to saturate downstream of 25D.

These observations of the field coherence allow for the separation of the field into four regions:

1) The first is the region where the BBSAN signature dominates. The frequency-dependent signature peaks at a lower frequency upstream and shifts to a higher frequency toward the sideline. Underneath the BBSAN, there is uncorrelated noise present, and so the coherence drops outside of the frequency band where the BBSAN peaks.

2) The second is the region of low coherence, upstream of the contribution of the aft radiation and downstream of the BBSAN component.

3) The third is the portion of the region of maximum radiation that shows traces of coherence with the BBSAN in region 1.

4) The fourth is the portion of the region of maximum radiation where the coherence with region 1 disappears until the end of the array.

Regions 1, 3, and 4 as identified by the field coherence can be qualitatively observed in the instantaneous pressure map of Fig. 1. Upstream radiation not originating from the nozzle exit is seen characteristic of BBSAN. Highly directional, planelike propagation of the waves originating from the plume upstream of the supersonic core are reminiscent of Mach wave radiation. Downstream of that, however, the radiated field looks significantly different. This observation motivates Sec. III.D, which uses the coherence between the pressures on the field array and the flow pressures along the nozzle lip line to identify source regions responsible for each of these identified field regions.

C. Flow Coherence

The advantage of investigating LESs as opposed to full-scale aircraft is that flow velocities and pressures are known. Thus, the same coherence analysis that was performed on the field can be repeated for the pressures along the nozzle lip line. Figure 5 shows the normalized sound pressure levels (left) as well as the normalized upstream coherence lengths (right) along the nozzle lip line. The wavelength used for normalization is the acoustic wavelength calculated using the local sound speed of $c = \sqrt{\gamma RT}$, where γ and T are, respectively, the ratio of specific heats and temperature (both of which vary with location), and R is the specific gas constant for air. The maximum levels along the lip line in Fig. 5 are between 3 and 15D downstream of the nozzle. Downstream of 15D, levels decrease at all frequencies, with the lowest frequencies decaying the slowest. At frequencies below 3.5 kHz and between 3 and 10D, there are vertical stripes in the level that appear to be due to the influence of the shock cells seen in the fluctuations in Fig. 2. Coherence lengths start small at the nozzle exit and quickly increase as the reference is moved downstream, with larger normalized coherence lengths at high frequency. From 3 to 10D, the coherence lengths are shortened at frequencies below 4 kHz. This is in the same region that vertical striations are visible in the level and where shock cells are present.

D. Coherence Between the Flow and the Field

Although coherence does not necessarily imply a cause and effect relationship, coherence between quantities in the flow and in the field show where similar information is included. First, $\mathbf{\Gamma}^2(f)$ is calculated between the sampled nozzle lip-line positions and the field array. Each column (or row) of $\mathbf{\Gamma}^2(f)$ then represents the coherence between a single reference on one array to the entirety of the other. To gain an idea of where the information in the field originates in the flow, for each point along the field array, the frequency-averaged coherence was calculated with the pressures along the nozzle lip line. Each colored line in Fig. 6a is the frequency-averaged coherence with respect to a particular reference point along the field array: the position of which is indicated by the color bar. For upstream references in the field (dark blues), the average coherence is low, with a small rise above the noise floor between $x/D = 5$ and 10 along the lip line. For references between $x/D = 5$ and 20 on the field array (light blues, teals, greens, and yellows), the coherence peaks, shifts downstream, and decays: all while maintaining a similar width. For references beyond $x/D = 20$ along the field array, the coherence peak widens, lowers in amplitude, and settles around $x/D = 15$ along the nozzle lip.

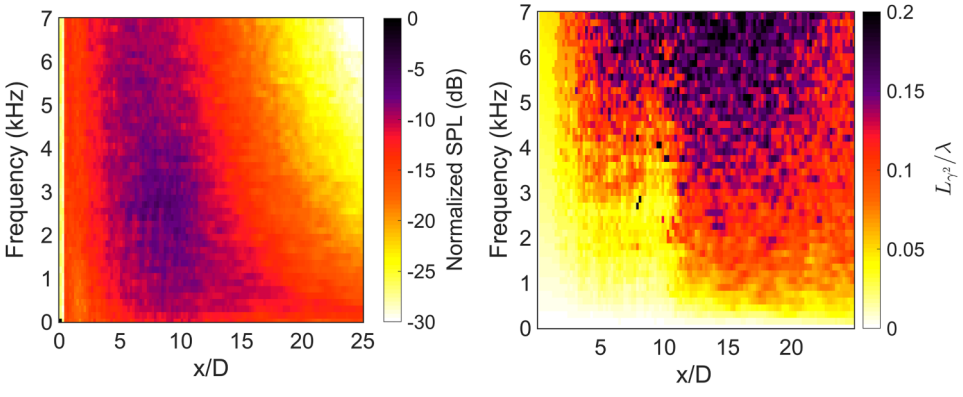

Fig. 5 Level and normalized coherence lengths of pressures along nozzle lip line.

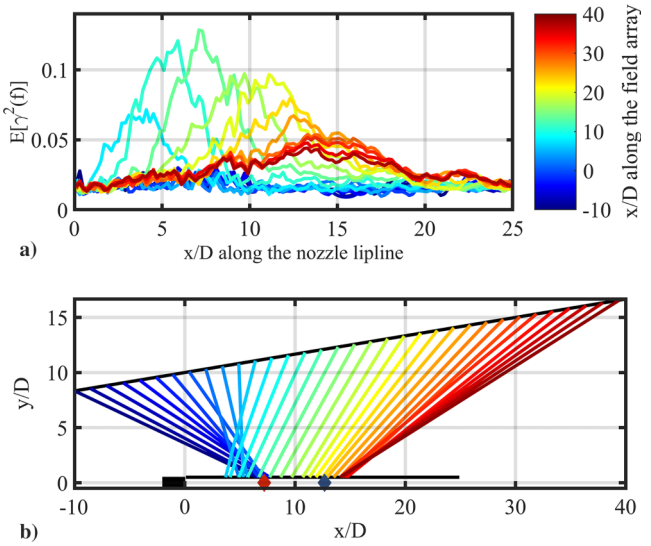

Fig. 6 Representations of a) frequency-averaged coherence between a particular reference point along field array (indicated by color) and all sampled points along nozzle lip line; and b) lines traced between points along the field array to the corresponding point of maximum frequency-averaged coherence along nozzle lip line.

To visualize this transfer of information from the flow pressures to the field pressures, Fig. 6b shows a schematic of the jet with lines traced from points along the field array to the corresponding points on the nozzle lip line where the frequency-averaged coherence (plotted in Fig. 6a) peaks. Because the curves in Fig. 6a are quite noisy, they were each smoothed and fit to a sum of two Gaussians, and the peak of the fitted curve was used. The peak of the coherence between field region 1 and the nozzle lip line falls between $x/D = 6$ and $x/D = 7.2$. The region of maximum radiation, which in Fig. 3 is seen as within the range $10 < x/D < 30$ on the field array, shares information with the flow region $5 < x/D < 14.5$. Aft of the region of maximum radiation ($x/D > 30$, the red lines), the peak of the coherence all originates from a compact region around $x/D = 15$ along the nozzle lip line; although, as seen in Fig. 6a, the relatively low coherence persists over a large area surrounding that point. Region 2 in the field is characterized by low field coherence, and subsequently has low coherence between the field and the nozzle lip line; it does not have a traceable corresponding flow region. Its influence is seen as extra disorder in the traced lines in the transition from region 1 to region 3.

The cyan, green, and yellow lines in Fig. 6b all share a similar slope and do not cross, suggesting that the radiation is superdirectional in that portion of the field. In conjunction with the coherence lengths observed in Figs. 3 and 5, the source could be described as a multiplicity of spatially ordered, overlapping source regions (not unlike wave packets), each with some sort of self-coherent phase relationship causing directional radiation (e.g., Mach wave radiation) that propagates to the field. Beyond the end of the supersonic core, however, the qualitative nature in the transfer of information from the near to the far field changes. The entirety of the field array beyond $x/D = 30$ contains information from an extended region centered around $x/D = 15$ (just beyond the end of the supersonic core) along the lip line. It appears that the nature of the sound radiating from this region of the nozzle lip line switches to be more omnidirectional instead of the highly directional radiation seen farther upstream. This switch explains why the aft portion of the field array has an increase in coherence as seen in Figs. 3 and 4. Omnidirectional radiation combined with the angle of the field array results in a small angle of incidence of the sound field at the far aft locations.

Based on Fig. 6, there appears to be three important regions in the flow:

1) The first is the potential core region, where both the BBSAN and the directional, aft radiation are originating.

2) The second is the region downstream of the potential core but upstream of the end of the supersonic core, where unidirectional radiation dominates.

3) The third is the region downstream of the supersonic core.

To look for phenomenological differences in these regions of the flow, three references were chosen along the nozzle lip line with which to calculate the coherence spectrum with the field array. The first two were chosen as where the field array references for Figs. 4c and 4d trace back to the nozzle lip line via the analysis in Fig. 6 ($x/D = 6.7$ and 11.1, respectively). The third reference is where the farthest aft point on the field array traces back to the nozzle lip line: $x/D = 14.1$. Figure 7 shows the coherence spectrum of the field array with these three reference points along the nozzle lip line, with the 6 dB-down region of the levels as displayed in Fig. 3 for scale.

Figure 7a shows the coherence between $x/D = 6.7$ on the nozzle lip line, representing flow region 1 and the entirety of the field array. This position in the flow transmits information to the acoustic field both upstream as BBSAN and downstream to the region of maximum radiation as Mach wave radiation. The transmitted information to the region of maximum radiation seems to segment itself into spatiospectral minima and maxima. This is the first hint of spatiospectral lobe separation in the region of maximum radiation seen in this dataset. Figure 7b shows the coherence spectrum of the field array with $x/D = 11.1$ at the nozzle lip line, which is a point between the end of the potential core and the end of the supersonic core, outside of the influence of shock cells. All evidence of coherence with the BBSAN region upstream disappears, and the spatiospectral region with appreciable coherence fills out the region of maximum radiation that is not covered in Fig. 7a, with the addition of some low-frequency content. Figure 7c uses a reference at $x/D = 14.1$, which seems to influence the field in a different way than Figs. 7a and 7b. The coherence consists of low frequencies (predominantly under 2 kHz) and is spread over a larger spatial region in the field. It does overlap with some of the low-frequency portion of Fig. 7b, which

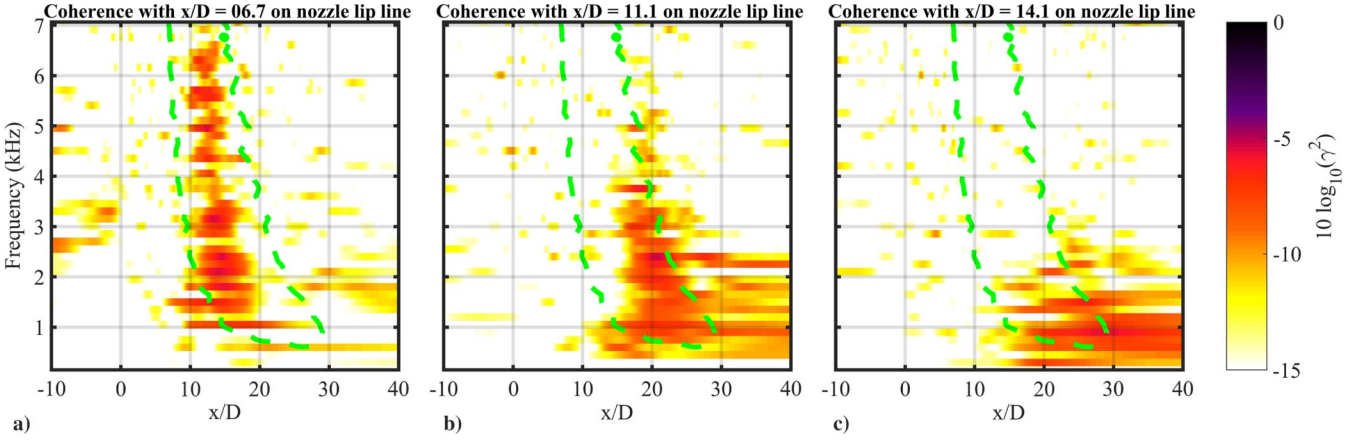

Fig. 7 Coherence between select points along nozzle lip line (marked in Fig. 2 by the hollow squares) and the field array.

suggests a gradual transition between the source mechanism responsible for the unidirectional radiation in Figs. 7a and 7b to this qualitatively different phenomenon in Fig. 7c. This gradual transition between source mechanisms is supported by the red lines in the frequency-averaged coherence in Fig. 6a. References at the end of the field array contain information from an extended region along the nozzle lip: on the order of 10 diameters wide.

The qualitative difference between the radiation originating upstream of and downstream of the supersonic core is easily described with the wave-packet analogy for jet noise [11]. If a wave-packet-type source description is used and is situated sufficiently upstream of the end of the supersonic core, then the phase relationship of the coherent wave packet would likely be supersonic, which results in efficient, directional Mach wave radiation. As the jet velocity decelerates with distance from the nozzle exit, however, the effective convective velocity decreases to subsonic, causing the phase speed of their wave-packet representation to be subsonic as well, resulting in only a portion of their wave-number spectrum radiating efficiently with a more omnidirectional directivity.

E. Coherence Analysis Summary

Combining the observations of the field, flow, and flow-to-field coherence calculations leads to a combination of four possible noise mechanisms in this simulation of a highly heated laboratory-scale jet: 1) BBSAN, 2) fine-scale turbulent structure noise, 3) Mach wave radiation from large-scale turbulent structures, and 4) large-scale turbulent structure noise. The spatial extents of these jet noise components along the nozzle lipline and the field array are summarized in Table 1.

The BBSAN component is a well-documented and -understood phenomenon that radiates primarily upstream (field region 1), although this work shows that portions of the aft radiation (field region 3) are coherent with the BBSAN. It is unknown if this is because the BBSAN radiates downstream as well as upstream or if the large-scale turbulent structures that actuate the shock cells imprint the shock cell information into the far field via their Mach wave radiation. Fine-scale turbulent structure noise is present as a background to the BBSAN components and dominant just upstream of the region of maximum radiation (field region 2). Mach wave radiation of large-scale turbulent structures is seen as nearly unidirectional radiation originating from the flow upstream of the end of the supersonic core (flow regions 1 and 2) and radiating to the upstream portion of the region of maximum radiation (field region 3). A qualitative description of this source mechanism is of spatially ordered, partially overlapping wave packets on the order of a few diameters in width with supersonic phase velocity. Although each wave packet would be self-coherent, coherence lengths are small (as seen in Fig. 5) because they are spatially compact.

The final noise mechanism discussed in this paper originates from region of the flow that is centered around the end of the supersonic core (region 3) but that extends both upstream into region 2 and even farther downstream. It contributes to the latter half of the region of maximum radiation all the way to the end of the field array (field region 4) and comprises low-frequency components, primarily under 2 kHz or a Strouhal number of about 0.12. A wave-packet description would be a set of spatially large self-coherent but mutually incoherent wave-packets that overlap, resulting in nonzero coherence lengths because of their size. Here, it is simply called large-scale turbulent structure noise, similar to previous work on this dataset [33] and other works that use LES to simulate high-temperature jets [35].

The two different source phenomena responsible for the aft radiation as seen in this work are remarkably similar to the results of Schmidt et al. [26], who analyzed LESs of subsonic and supersonic cold jets using SPOD and resolvent analysis. They found that the SPOD and resolvent modes take on wave-packet shapes, which are qualitatively similar to the two source mechanisms described here, and are dubbed Kelvin–Helmholtz type or Orr type. The Kelvin–Helmholtz-type wave packets originate along the upstream shear layer and are responsible for the majority of the radiation, whereas the Orr-type wave packets are primarily active downstream of the potential core at lower frequencies. The Orr-type modes are not low rank but are extended over a region and require many overlapping suboptimal modes to predict the overall response. The physical mechanism attributed to these modes is the Orr mechanism [36]. The characterization of this superposition of overlapping self-coherent modes to produce the field is important to linear analyses [30], which have had difficulty reproducing the far aft low-frequency radiation. Adding coherence decay to wave-packet models [44] to the nominally coherent linear analyses is required to match the radiated field at large aft angles and low frequencies.

Table 1 Summary of jet noise components observed by coherence analysis and their estimated regions along the nozzle lip line and field arrays

Noise component	Flow extent	Field extent
BBSAN	$6 < x/D < 7.2$	$x/D < 2$
Fine-scale turbulent structure noise	— —	$2 < x/D < 5$
Mach wave radiation	$x/D < 12.67$	$5 < x/D < 25$
Large-scale turbulent structure noise	$7.2 < x/D < 20$	$20 < x/D$

IV. Comparison to the F-35B

High-fidelity measurements of the jet noise produced by military aircraft have been achieved in recent years [12,13]. Analyses of near-field measurements of the noise from a tied-down F-35B aircraft have shown significant deviation from the traditional two-source model [17,19], and they are phenomenologically compared to the LES of the highly heated jet here.

The measurement of the F-35B was performed at Edwards Air Force Base in 2013 [13]. The aircraft was tied down to a concrete runup pad and its engine cycled from 13% ETR up through 150% ETR. Engine powers greater than 100% ETR are due to the addition of afterburner. The nozzle of the engine was 2.0 m from the ground and had a nominal 1 m diameter, although the exact nozzle diameter changed with engine condition. The origin of the coordinate system used in this study is at the nozzle exit with the jet plume faced down the positive x axis. The y axis is the distance from the jet centerline, and the z axis is the height above the ground. The array was laid out to the left side of the aircraft as shown in Ref. [13]; although, for convenience, it is mirrored to show it on the right side of the aircraft. This study focuses on a 32-m-long 71-element (0.45 m interelement spacing) linear ground array placed approximately parallel to the shear layer, which is shown in Fig. 8. The recorded 30-s-time waveforms (204.8 kHz sampling frequency) were split into multiple blocks with a 50% overlap, windowed with a Hann function, and then the Fourier transform was applied to each block. Swift et al. [19] analyzed the full high-resolution dataset. For this work, to be able to compare more closely with the LES of the heated laboratory-scale jet, the block size was adjusted to give a frequency resolution of 15 Hz and only 97 blocks were used.

The temperature ratio in the LES analyzed in this study was chosen to be similar to a tactical aircraft operating at afterburner, and so the 150% ETR case of the F-35B measurement is studied here. The only attempt to scale either dataset for comparison was the normalization of levels and the choices of frequency range and resolution. The normalized spectrum measured along the array is displayed in the left pane of Fig. 9. The BBSAN is seen upstream starting at 350 Hz, increasing to 700 Hz at $x = 5$m. The directional portion of the turbulent mixing noise dominates from 5 to 30 m downstream.

The calculated upstream coherence lengths for the F-35B measurement were first shown in Ref. [19] and are repeated here in Fig. 9 (although this study uses a coarser frequency resolution for comparison to the LES). The coherence lengths are large upstream in the 300–600 Hz band due to the presence of the BBSAN, become uniformly smaller in the region dominated by sideline radiation, and increase again in the region of maximum radiation. Aft of the region of maximum radiation, at high frequencies at the end of the array, the frequencies above 350 Hz begin to saturate; this is likely due to the array measuring a progressive wave field because it is large compared to the aeroacoustic sources. A striking feature of Fig. 9 is the oscillation in the level and the coherence length in the region of maximum radiation. This oscillation in the region of maximum radiation can modulate the level on the order of

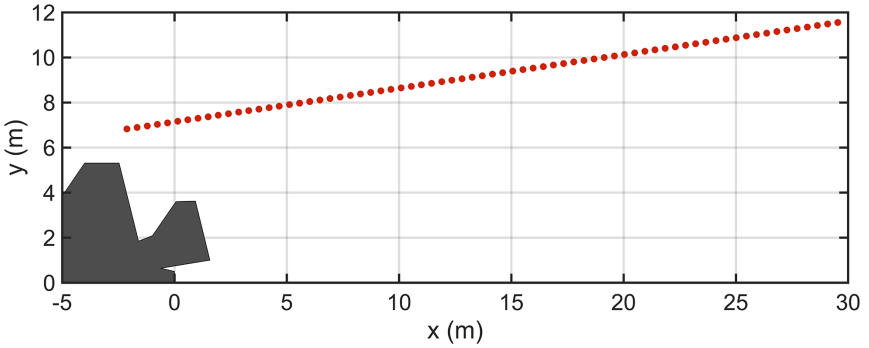

Fig. 8 Schematic of the linear ground array used to measure the jet noise field of the F-35B.

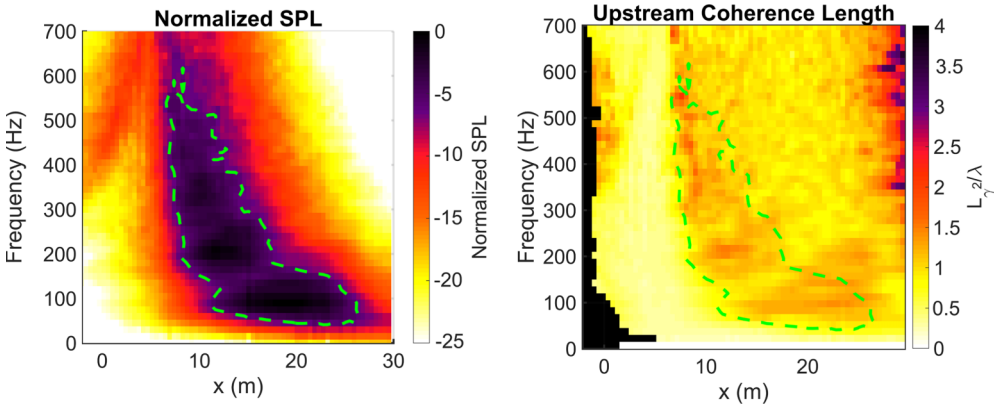

Fig. 9 Normalized SPL and coherence lengths measured by the array in Fig. 8 while the F-35B aircraft was operating at 150% ETR.

5 dB and double the value of L_{γ^2}/λ. The oscillations in the spatiospectral domain are called spatiospectral lobes. These spatiospectral lobes were investigated more in depth by Refs. [17,19,47]. They represent either a dual peak in the frequency spectrum at a single measurement location or a split directivity pattern in the field at a single frequency.

Despite the fact that the operating conditions and nozzle geometries of this LES dataset and the F-35 are not the same, general comparisons of the levels and coherence lengths are still favorable. All the coherence length trends appear to hold generally, except that L_{γ^2}/λ is slightly larger for the LES than for the F-35. The largest difference is, of course, the spatiospectral lobe content in the F-35. It is unknown at this point why the LES does not contain this phenomenon. In Fig. 3, the coherence lengths inside and just aft of the region of maximum radiation above 2 kHz are about the same; in Fig. 9, for the F-35, the coherence lengths are larger at the spatiospectral lobe peaks (almost as if an additional coherent noise source were superimposed on top of the general field). However, the horizontal portion of the farthest aft lobe of the F-35 matches the low-frequency aft frequency content seen in the LES.

Since the F-35 measurement does not provide information about the flow, other studies have used acoustic inverse methods in an attempt to identify source regions for the noise measured along this array. Leete et al. [17] used an advanced acoustical holography technique to reconstruct the acoustic field of the F-35 from this same dataset from the nozzle lip line out to a large area surrounding the aircraft. Although limited to frequencies below 400 Hz, they were able to trace individual spatiospectral lobes to their apparent origins along the jet centerline. The low-frequency far aft spatiospectral lobe was traced to a source location downstream of $x/D = 12$, whereas the next two lowest lobes were traced to the an upstream region between $x/D = 5$ and $x/D = 10$. The low-frequency lobe also had an appreciably shallower directivity than the two higher lobes. When compared with the current work, the lowest-frequency farthest aft lobe could be identified as large-scale turbulent structure-type radiation, whereas the higher-frequency lobes could be identified as Mach wave radiation.

V. Conclusions

Level and coherence analyses of the simulated noise from a highly heated jet lead to the identification of distinct regions of interest in the flow and in the field. Field region 1 is characterized by the presence of the BBSAN, where the spatially dependent self-coherent spectra appear upstream. The BBSAN information originates from the nozzle lip line in flow region 1, which is upstream of the end of the potential core. Field region 2 is the region of low coherence toward the sideline of the jet, just upstream of the region of maximum radiation. Field region 3 is the upstream portion of the region of maximum radiation. It is self-coherent and partially coherent with the BBSAN upstream. It originates from flow region 1 as well as flow region 2, which is between the end of the potential and supersonic cores. Field region 4 begins with the low-frequency portion of the region of maximum radiation and extends downstream to the end of the array, and it contains information from flow region 2 as well as region 3, which is downstream of the supersonic core.

Analysis of the transfer of information between the nozzle lip line and the field array illuminates four different potential noise mechanisms at play in this jet: broadband shock-associated noise, fine-scale turbulent structure noise, Mach wave radiation of large-scale turbulent structures, and large-scale turbulent structure noise. Traditionally, the directional radiation in the aft direction has been attributed solely to the Mach wave radiation of large-scale turbulent structures. It is seen with this LES that the large-scale turbulent structure noise originating from the supersonic portion of the flow transmits its energy more efficiently to the field in the characteristic unidirectional pattern associated with Mach wave radiation. However, as the jet velocity decreases with distance from the nozzle, a qualitatively new noise source begins to appear where the frequency content shifts lower and the directivity becomes more omnidirectional. This noise source is centered just downstream of the end of the supersonic core, although it is on the order of 10 diameters wide.

Although the idea of multiple noise production mechanisms contributing to the aft radiation is heartening for understanding the spatiospectral lobes measured in the F-35 field, the observations of the LES only show a smooth transition from one noise production

mechanism to another, which does not generate a split directivity in the field or a dual peak in the spectrum. However, there are qualitative similarities between the farthest aft lobe of the F-35 and the large-scale turbulent structure noise observed in this study and the coherence calculated between a point in the flow where shock cells are present does split the coherence of Mach wave radiation component into what appears to be spatiospectral lobe shapes (see Fig. 7a). At this point, bringing LES of a laboratory-scale jet to high temperatures (designed to be in the same regime as high-performance military aircraft operating at afterburner) does not account for all of the spatiospectral lobe content that is observed in the F-35. Additional laboratory-scale tests or LESs operating at even more realistic high-performance military aircraft conditions are needed to fully understand the spatiospectral characteristics of the F-35.

Acknowledgments

This research was supported in part by the U.S. Office of Naval Research through the Jet Noise Reduction Project. The authors also gratefully acknowledge funding for the F-35 measurements provided through the F-35 Joint Program Office and the U.S. Air Force Research Laboratory (USAFRL). K. M. Leete was funded by an appointment to the Student Research Participation Program at the U.S. Air Force Research Laboratory, 711th Human Performance Wing, Human Effectiveness Directorate, Warfighter Interface Division, Battlespace Acoustics Branch administered by the Oak Ridge Institute for Science and Education through an interagency agreement between the U.S. Department of Energy and the USAFRL. (Distribution A: Approved for public release; distribution unlimited. Cleared 09/27/2019 JSF19-903).

References

[1] Tam, C., Golebiowski, M., and Seiner, J., "On the Two Components of Turbulent Mixing Noise from Supersonic Jets," *Aeroacoustics Conference*, AIAA Paper 1996-1716, 1996. https://doi.org/10.2514/6.1996-1716

[2] Bogey, C., and Bailey, C., "An Analysis of the Correlations Between the Turbulent Flow and the Sound Pressure Fields of Subsonic Jets," *Journal of Fluid Mechanics*, Vol. 583, July 2007, pp. 71–97. https://doi.org/10.1017/S002211200700612X

[3] Panda, J., and Seasholtz, R. G., "Experimental Investigation of Density Fluctuation in High-Speed Jets and Correlation with Generated Noise," *Journal of Fluid Mechanics*, Vol. 450, Jan. 2002, pp. 97–130. https://doi.org/10.1017/S002211200100622X

[4] Panda, J., Seasholtz, R. G., and Elam, K. A., "Investigation of Noise Sources in High-Speed Jets via Correlation Measurements," *Journal of Fluid Mechanics*, Vol. 537, Aug. 2005, pp. 349–385. https://doi.org/10.1017/S0022112005005148

[5] Viswanathan, K., Underbrink, J. R., and Brusniak, L., "Space-Time Correlation Measurements in Nearfields of Jets," *AIAA Journal*, Vol. 49, No. 8, 2011, pp. 1577–1599. https://doi.org/10.2514/1.J050750

[6] Crow, S. C., and Champagne, F. H., "Orderly Structures in Jet Turbulence," *Journal of Fluid Mechanics*, Vol. 48, No. 3, 1971, pp. 547–591. https://doi.org/10.1017/S0022112071001745

[7] Brown, G. L., and Roshko, A., "On Density Effects and Large Structures in Turbulent Mixing Layers," *Journal of Fluid Mechanics*, Vol. 64, No. 4, 1974, pp. 775–816. https://doi.org/10.1017/S002211207400190X

[8] Tam, C. K. W., and Auriault, L., "Jet Mixing Noise from Fine-Scale Turbulence," *AIAA Journal*, Vol. 37, No. 2, 1999, pp. 145–153. https://doi.org/10.2514/2.691

[9] Tam, C. K. W., Viswanathan, K., Ahuja, K. K., and Panda, J., "The Sources of Jet Noise: Experimental Evidence," *Journal of Fluid Mechanics*, Vol. 615, Nov. 2008, pp. 253–292. https://doi.org/10.1017/S0022112008003704

[10] Tam, C. K. W., and Chen, K. C., "A Statistical Model of Turbulence in Two-Dimensional Mixing Layers," *Journal of Fluid Mechanics*, Vol. 92, No. 2, 1979, pp. 303–326. https://doi.org/10.1017/S002211207900063X

[11] Jordan, P., and Colonius, T., "Wave Packets and Turbulent Jet Noise," *Annual Review of Fluid Mechanics*, Vol. 45, No. 1, 2013, pp. 173–195. https://doi.org/10.1146/annurev-fluid-011212-140756

[12] Wall, A. T., Gee, K. L., James, M. M., Bradley, K. A., McInerny, S. A., and Neilsen, T. B., "Near-Field Noise Measurements of a High Performance Military Jet Aircraft," *Noise Control Engineering Journal*, Vol. 60, No. 4, 2012, pp. 421–434. https://doi.org/10.3397/1.3701021

[13] James, M. M., Salton, A. R., Downing, J. M., Gee, K. L., Neilsen, T. B., Reichman, B. O., McKinley, R., Wall, A. T., and Gallagher, H., "Acoustic Emissions from F-35 Aircraft During Ground Run-Up," *21st AIAA/CEAS Aeroacoustics Conference*, AIAA Paper 2015-2375, 2015. https://doi.org/10.2514/6.2015-2375

[14] Tam, C. K., Aubert, A. C., Spyropoulos, J. T., and Powers, R. W., "On the Dominant Noise Components of Tactical Aircraft: Laboratory to Full Scale," *23rd AIAA/CEAS Aeroacoustics Conference*, AIAA Paper 2017-3516, 2017. https://doi.org/10.2514/6.2017-3516

[15] Neilsen, T. B., Gee, K. L., Wall, A. T., and James, M. M., "Similarity Spectra Analysis of High-Performance Jet Aircraft Noise," *Journal of the Acoustical Society of America*, Vol. 133, No. 4, 2013, pp. 2116–2125. https://doi.org/10.1121/1.4792360

[16] Neilsen, T. B., Vaughn, A. B., Gee, K. L., Swift, S. H., Wall, A. T., Downing, J. M., and James, M. M., "Three-Way Spectral Decompositions of High-Performance Military Aircraft Noise," *AIAA Journal*, Vol. 57, No. 8, 2019, pp. 3467–3479. https://doi.org/10.2514/1.J057992

[17] Leete, K. M., Wall, A. T., Gee, K. L., Neilsen, T. B., James, M. M., and Downing, J. M., "Dependence of High-performance Military Aircraft Noise on Frequency and Engine Power," *2018 AIAA/CEAS Aeroacoustics Conference*, AIAA Paper 2018-2826, 2018. https://doi.org/10.2514/6.2018-2826

[18] Harker, B. M., Neilsen, T. B., Gee, K. L., Wall, A. T., and James, M. M., "Spatiotemporal-Correlation Analysis of Jet Noise from a High-Performance Military Aircraft," *AIAA Journal*, Vol. 54, No. 5, 2016, pp. 1554–1566. https://doi.org/10.2514/1.J054442

[19] Swift, S. H., Gee, K. L., Neilsen, T. B., Wall, A. T., Downing, J. M., and James, M. M., "Spatiotemporal-Correlation Analysis of Jet Noise from a Round Nozzle High-Performance Aircraft," *2018 AIAA/CEAS Aeroacoustics Conference*, AIAA Paper 2018-3938, 2018. https://doi.org/10.2514/6.2018-3938

[20] Seiner, J. M., Ponton, M. K., Jansen, B. J., and Lagen, N. T., "The Effects of Temperature on Supersonic Jet Noise Emission," *14th DGLR/AIAA Aeroacoustics Conference*, Vol. 1, Paper A93-19126 05-71, 1992, pp. 295–307.

[21] Long, D., "Jet Noise Source Location via Acoustic Holography and Shadowgraph Imagery," *14th AIAA/CEAS Aeroacoustics Conference (29th AIAA Aeroacoustics Conference)*, AIAA Paper 2008-2888, 2008. https://doi.org/10.2514/6.2008-2888

[22] Bodony, D. J., and Lele, S. K., "Current Status of Jet Noise Predictions Using Large-Eddy Simulation," *AIAA Journal*, Vol. 46, No. 2, 2008, pp. 364–380. https://doi.org/10.2514/1.24475

[23] Bres, G. A., and Lele, S. K., "Modelling of Jet Noise: A Perspective from Large-Eddy Simulations," *Philosophical Transactions of the Royal Society of London, Series A: Mathematical, Physical and Engineering Sciences*, Vol. 377, No. 2159, 2019, Paper 20190081. https://doi.org/10.1098/rsta.2019.0081

[24] Taira, K., Brunton, S. L., Dawson, S. T. M., Rowley, C. W., Colonius, T., McKeon, B. J., Schmidt, O. T., Gordeyev, S., Theofilis, V., and Ukeiley, L. S., "Modal Analysis of Fluid Flows: An Overview," *AIAA Journal*, Vol. 55, No. 12, 2017, pp. 4013–4041. https://doi.org/10.2514/1.J056060

[25] Unnikrishnan, S., and Gaitonde, D. V., "Acoustic, Hydrodynamic and Thermal Modes in a Supersonic Cold Jet," *Journal of Fluid Mechanics*, Vol. 800, Aug. 2016, pp. 387–432. https://doi.org/10.1017/jfm.2016.410

[26] Schmidt, O. T., Towne, A., Rigas, G., Colonius, T., and Brès, G. A., "Spectral Analysis of Jet Turbulence," *Journal of Fluid Mechanics*, Vol. 855, Nov. 2018, pp. 953–982. https://doi.org/10.1017/jfm.2018.675

[27] Schmid, P. J., and Sesterhenn, J., "Dynamic Mode Decomposition of Numerical and Experimental Data," *Journal of Fluid Mechanics*, Vol. 656, Aug. 2010, pp. 5–28. https://doi.org/10.1017/S0022112010001217

[28] Theofilis, V., "Global Linear Instability," *Annual Review of Fluid Mechanics*, Vol. 43, No. 1, 2011, pp. 319–352. https://doi.org/10.1146/annurev-fluid-122109-160705

[29] Towne, A., Schmidt, O. T., and Colonius, T., "Spectral Proper Orthogonal Decomposition and Its Relationship to Dynamic Mode Decomposition and Resolvent Analysis," *Journal of Fluid Mechanics*, Vol. 847, July 2018, pp. 821–867. https://doi.org/10.1017/jfm.2018.283

[30] Jordan, P., Zhang, M., Lehnasch, G., and Cavalieri, A. V., "Modal and Non-Modal Linear Wavepacket Dynamics in Turbulent Jets," *23rd*

AIAA/CEAS Aeroacoustics Conference, AIAA Paper 2017-3379, 2017. https://doi.org/10.2514/6.2017-3379.

[31] Liu, J., Corrigan, A. T., Kailasanath, K., and Gutmark, E. J., "Impact of Chevrons on Noise Source Characteristics In Imperfectly Expanded Jet Flows," *21st AIAA/CEAS Aeroacoustics Conference*, AIAA Paper 2015-2835, 2015. https://doi.org/10.2514/6.2015-2835

[32] Liu, J., Corrigan, A. T., Kailasanath, K., and Taylor, B. D., "Impact of the Specific Heat Ratio on the Noise Generation in a High-Temperature Supersonic Jet," *54th AIAA Aerospace Sciences Meeting*, AIAA Paper 2016-2125, 2016. https://doi.org/10.2514/6.2016-2125

[33] Liu, J., Kailasanath, K., and Gutmark, E. J., "Similarity Spectra Analysis in Highly Heated Supersonic Jets Using Large-Eddy Simulations," *55th AIAA Aerospace Sciences Meeting*, AIAA Paper 2017-0926, 2017. https://doi.org/10.2514/6.2017-0926

[34] Chen, S., Gojon, R., and Mihaescu, M., "High-Temperature Effects on Aerodynamic and Acoustic Characteristics of a Rectangular Supersonic Jet," *2018 AIAA/CEAS Aeroacoustics Conference*, AIAA Paper 2018-3303, 2018. https://doi.org/10.2514/6.2018-3303

[35] Chen, S., and Mihaescu, M., "Nozzle Pressure Ratio Effects on Aerodynamics and Acoustics of a Highly-Heated Rectangular Supersonic Jet," *25th AIAA/CEAS Aeroacoustics Conference*, AIAA Paper 2019-2753, 2019. https://doi.org/10.2514/6.2019-2753

[36] Tissot, G., Lajús, F. C., Cavalieri, A. V. G., and Jordan, P., "Wave Packets and Orr Mechanism in Turbulent Jets," *Physical Review Fluids*, Vol. 2, No. 9, 2017, Paper 093901. https://doi.org/10.1103/PhysRevFluids.2.093901

[37] Löhner, R., Morgan, K., Peraire, J., and Vahdati, M., "Finite Element Flux-Corrected Transport (FEM-FCT) for the Euler and Navier-Stokes Equations," *International Journal for Numerical Methods in Fluids*, Vol. 7, No. 10, 1987, pp. 1093–1109. https://doi.org/10.1002/(ISSN)1097-0363

[38] Lyrintzis, A. S., "Surface Integral Methods in Computational Aeroacoustics-From the (CFD) Near-Field to the (Acoustic) Far-Field," *International Journal of Aeroacoustics*, Vol. 2, No. 2, 2003, pp. 95–128. https://doi.org/10.1260/147547203322775498

[39] Liu, J., Kailasanath, K., Boris, J., Heeb, N., Munday, D., and Gutmark, E., "Effect of Nozzle-Exit Flow Conditions on the Flow and Acoustic Properties of Imperfectly Expanded Supersonic Jets," *18th AIAA/CEAS Aeroacoustics Conference (33rd AIAA Aeroacoustics Conference)*, AIAA Paper 2012-2161, 2012. https://doi.org/10.2514/6.2012-2161

[40] Walton, J. T., and Burcham, F. W., Jr., "Exhaust-Gas Pressure and Temperature Survey of F404-GE-400 Turbofan Engine," NASA TM 88273, 1986, https://ntrs.nasa.gov/archive/nasa/casi.ntrs.nasa.gov/19880010923.pdf.

[41] Bres, G. A., Towne, A., and Lele, S. K., "Investigating the Effects of Temperature Non-Uniformity on Supersonic Jet Noise with Large-Eddy Simulation," *25th AIAA/CEAS Aeroacoustics Conference*, AIAA Paper 2019-2730, 2019. https://doi.org/10.2514/6.2019-2730

[42] Tam, C. K. W., "Mach Wave Radiation from High-Speed Jets," *AIAA Journal*, Vol. 47, No. 10, 2009, pp. 2440–2448. https://doi.org/10.2514/1.42644

[43] Piersol, A. G., and Bendat, J. S., *Random Data: Analysis and Measurement Procedures*, 4th ed., Wiley-Interscience, New York, 1986, p. 306.

[44] Maia, I. A., Jordan, P., Cavalieri, A. V. G., and Jaunet, V., "Two-Point Wavepacket Modelling of Jet Noise," *Proceedings of the Royal Society of London, Series A: Mathematical, Physical and Engineering Sciences*, Vol. 475, No. 2227, 2019, Paper 20190199. https://doi.org/10.1098/rspa.2019.0199

[45] Harker, B. M., Gee, K. L., Neilsen, T. B., Wall, A. T., and James, M. M., "Beamforming-Based Wavepacket Model for Noise Environment Predictions of Tactical Aircraft," *23rd AIAA/CEAS Aeroacoustics Conference*, AIAA Paper 2017-4048, 2017. https://doi.org/10.2514/6.2017-4048

[46] Tam, C., "Stochastic Model Theory of Broadband Shock Associated Noise from Supersonic Jets," *Journal of Sound and Vibration*, Vol. 116, No. 2, 1987, pp. 265–302. https://doi.org/10.1016/S0022-460X(87)81303-2

[47] Wall, A. T., Gee, K. L., Leete, K. M., Neilsen, T. B., Stout, T. A., and James, M. M., "Partial-Field Decomposition Analysis of Full-Scale Supersonic Jet Noise Using Optimized-Location Virtual References," *Journal of the Acoustical Society of America*, Vol. 144, No. 3, 2018, pp. 1356–1367. https://doi.org/10.1121/1.5053580

L. Ukeiley
Associate Editor